



Research papers

Projections and uncertainty decomposition in CMIP6 models for extreme precipitation scaling rates



Min Sothearith, Kuk-Hyun Ahn*

Department of Civil and Environmental Engineering, Kongju National University, Cheon-an, South Korea

ARTICLE INFO

This manuscript was handled by A. Bardossy, Editor-in-Chief, with the assistance of Jie Chen, Associate Editor

Keywords:

Scaling rate
Climate projection uncertainty
Uncertainty contribution
Coupled Model Intercomparison Project (CMIP)
phase 5 (CMIP5) and phase 6 (CMIP6)

ABSTRACT

As temperatures rise, extreme precipitation is expected to intensify, following the Clausius–Clapeyron relation, which indicates a 7 % increase in extreme precipitation for every 1 °C rise in temperature. However, recent studies reveal considerable uncertainty in estimating the rate of change in extreme precipitation (scaling rate), especially in future projections. This study aims to quantify the contribution to scaling rate projections by focusing on three primary factors: Global Circulation Models (GCMs), future emission scenarios, and scaling methods. Additionally, we examine the minimum number of GCMs required for robust analysis and compare the uncertainty contributions between CMIP5 and CMIP6 to assess differences between the two CMIP generations. Our findings reveal substantial variations in the projected global and regional scaling rates, along with significant temporal changes. While GCMs are the primary source of uncertainty in scaling rates, using fewer GCMs tends to underestimate their influence on uncertainty and overestimate the impact of other sources. Furthermore, to ensure robust results, we recommend using at least nine GCMs in scaling rate projections, though some regional variations may still occur. Lastly, our evaluation reveals that while both CMIP5 and CMIP6 show comparable spatial distributions, CMIP5 exhibits greater uncertainty. Although global averages reveal only minor differences in uncertainty contributions from each source between the two generations, significant regional variations, particularly in the northeastern Eurasian region, have been identified. We believe that this comprehensive understanding of uncertainty in scaling rates will enhance future projections and support the development of effective strategies for managing extreme precipitation in future water policy planning.

1. Introduction

A warmer atmosphere has a greater ability to hold water vapor than a colder one, based on a thermodynamic principle first proposed by Clapeyron (1834) and further developed by Clausius (1850). Theoretically, the water vapor content increases exponentially by about 7 % per 1 °C rise in temperature, a relationship known as the Clausius–Clapeyron relation (CC scaling). An increase in the amount of water vapor in the atmosphere means that there is more precipitable water during precipitation events, thereby making the extreme precipitation event more intense (Trenberth et al., 2003). Numerous studies have found that the rate of change in extreme precipitation with changing temperatures (scaling rate) aligns with CC scaling (Allan and Soden, 2008; Fischer and Knutti, 2016; Li et al., 2021). The scaling rate has served as a guiding principle for better understanding extreme precipitation in a warming climate (O’Gorman, 2015). For instance, Lenderink and Attema (2015) used scaling rate to develop climate scenarios for local extreme

precipitation in the Netherlands. Furthermore, extreme precipitation has been closely linked to hydrometeorological disasters such as floods, landslides, and other climate-related hazards (Buathongkhue et al., 2024; Deng et al., 2024; Yanfatriani et al., 2024). Therefore, given the expected rise in temperature over time due to climate change (IPCC, 2021), understanding the scaling rates is essential for developing effective adaptation and mitigation strategies.

Many studies have been conducted to investigate the scaling rates regionally and globally. Some have relied on historical data (Ali et al., 2018; Hardwick Jones et al., 2010; Westra et al., 2014; Zhang et al., 2017), while others have used projected data from climate models (John et al., 2022; Kharin et al., 2013; Pfahl et al., 2017; Trenberth, 2011; O’Gorman and Schneider, 2009). However, these studies revealed significant discrepancies in estimated scaling rates compared to the expected CC scaling. Even when using observed data, variations in estimated scaling rates may arise from differences in statistical modeling methods and regional moisture limitations. However, these variations

* Corresponding author.

E-mail address: ahnkukhyun@kongju.ac.kr (K.-H. Ahn).

can potentially be reduced by pooling grid data to increase sample sizes and incorporating dewpoint temperature as a scaling variable (Ali et al., 2022, 2018; Fowler et al., 2021; Martinkova and Kysely, 2020). Ali et al. (2018) concluded that dewpoint temperature delivers more consistent scaling rate after comparing several temperature variables. On the other hand, for the projection studies, the variations of estimated scaling rates are more severe. To be specific, those studies face additional uncertainties from climate model simulation due to variations in climate model structures and future emission scenarios (John et al., 2022; Kharin et al., 2013, 2007; Li et al., 2021; O'Gorman and Schneider, 2009).

In future projection studies, Global Circulation Models (GCMs) have been the primary climate models employed by scientists to access future climate conditions through computational simulation (Eyring et al., 2016). GCMs have been made available through the Coupled Model Intercomparison Project (CMIP) under the World Climate Research Programme (WCRP) in different generations (Sansom et al., 2013). Currently, CMIP is undergoing its sixth phase (CMIP6). CMIP6 integrates Shared Socioeconomic Pathways (SSP) scenarios, which encompass not just greenhouse gas emissions but also socioeconomic factors like population growth, rate of technology development, and many other relevant factors (O'Neill et al., 2016). Nonetheless, the lack of comprehensive understanding regarding future emissions introduces uncertainty in these future emission scenarios (Riahi et al., 2017). Moreover, the diverse model structure of individual GCMs contributes significantly to uncertainty dispersion in future climate projections (Knutti et al., 2019). This is especially notable in CMIP6, where the model spread is higher than in previous generations due to its more comprehensive consideration (Lehner et al., 2020; Wu et al., 2024; Zhang and Chen, 2021; Liang-Liang et al., 2022). For study on scaling rate uncertainty, John et al. (2022) quantified the uncertainty in scaling rates among CMIP6 GCMs and discovered a significant variation among the models, particularly in the tropical region. Similarly, Pfahl et al. (2017) utilized GCMs from CMIP5 and confirmed that future scaling rates will not remain constant. Hence, the estimated scaling rate will be uncertain due to GCMs and future emission scenarios, but the contribution to the overall uncertainty in estimating scaling rates for future projection has yet to be fully assessed.

An additional layer of uncertainty in estimating scaling rates arises from the diversity of statistical modeling methods developed, as scientists have chosen different methods in their studies. For instance, Lenderink and van Meijgaard (2008) introduced the equal bin width binning method, which was also employed by Lenderink et al. (2011), Park and Min (2017), and Wasko and Sharma (2014). This method categorizes precipitation data by temperature into equal-width bins. It then selects a high quantile value (e.g., 95th, 99th, or 99.5th) of precipitation from each bin and the temperature midpoint of each bin as the representative pair. Finally, it fits the temperature-extreme precipitation pairs to a linear model to calculate the scaling rate. By modifying the aforementioned method, Hardwick Jones et al. (2010) binned the precipitation data by temperature with each bin having equal precipitation data distributed. This method has been followed by numerous studies, as seen in Mishra et al. (2012), Yoo and Ahn (2023), and Ali et al. (2018). Selecting a hyperparameter is required before applying both binning methods. For the equal bin width method, the bin width must be specified, with 2 °C being a common choice in many studies (Lenderink et al., 2011; Park and Min, 2017; Wasko and Sharma, 2014). Similarly, for the equal sample sizes method, the number of bins must be determined, with options such as 12, 15, 20, or 30, as seen in various studies (Mishra et al., 2012; Yoo and Ahn, 2023; Ali et al., 2018; Ali and Mishra, 2017). However, it is worth noting that Pumo et al. (2019) found that the choice of the number of bins does not significantly impact scaling rate estimations. In addition to binning methods, Wasko and Sharma (2014) proposed the use of quantile regression to detect the relationship between high-quantile precipitation and temperature without having to bin the data first. Subsequently, many studies, such as Molnar et al.

(2015), and Schroeer and Kirchengast (2018), also employed quantile regression in their scaling rate estimation. Regardless of the different scaling methods utilized in various studies, comparing different scaling studies proves challenging due to methodological disagreements (Fowler et al., 2021), leading to inherent uncertainty when determining the scaling rate, especially with a small sample size (Ali et al., 2022; Wasko and Sharma, 2014).

As previously mentioned, three sources—future emission scenarios, GCMs, and scaling methods—may impact the estimation of scaling rates based on climate model simulation data. However, to the best of the authors' knowledge, the specific contribution of each source to overall uncertainty has not been quantified in existing literature. While the concept of decomposing overall uncertainty into contributions from different sources in projected climatic conditions has been extensively explored in studies like projected precipitation and temperature (Hawkins and Sutton, 2009; Lehner et al., 2020; Yip et al., 2011), and hydrological variables (Wang et al., 2020; Wu et al., 2024), as well as extreme events such as drought (Ji et al., 2024), the decomposition of uncertainty in extreme precipitation scaling rates remain unexamined. Understanding the uncertainty contribution is important for future climate model development and a clear scientific communication (Lehner et al., 2020). Therefore, it is imperative to investigate the contribution of each source to the overall uncertainty in estimating scaling rates.

To address gaps in existing literature, this study aims to quantify the contributions of GCMs, future emission scenarios, and modeling methods to the uncertainty in estimated scaling rates on a global scale. While many GCMs are accessible, employing a large number of them may impose computational burdens. As such, we will also investigate the necessary number of GCMs for robust results, drawing on insights from Wang et al. (2020) and Zhang et al. (2023), which emphasize the importance of selecting an appropriate number of GCMs to ensure the robustness of the uncertainty decomposition framework. Additionally, we will compare the uncertainty decomposition of Coupled Model Intercomparison Project Phase 5 (CMIP5) with CMIP6 to understand differences between these two phases, focusing on the contributions from each uncertainty source. To be specific, we will address four scientific questions: (1) What are the projected scaling rates and their variations in the long-term period from 2041 to 2090? (2) How does each source contribute to the overall uncertainty in scaling rates? (3) How many GCMs are necessary for a robust uncertainty decomposition? (4) What are the differences in uncertainty contributions from each source between CMIP5 and CMIP6? The rest of the paper is structured as follows. We begin by introducing the models and methods used in this study in Section 2. In Section 3, we present the results, including the global and regional uncertainty contributions from each source. Finally, Section 4 presents our discussions, while Section 5 offers our conclusions, both aiming to provide more robust scaling rate projections.

2. Data and methods

This study utilized three sources of uncertainty in the scaling rate estimation for future simulations: future emission scenarios, GCMs, and scaling methods (refer to Fig. 1). The modeling chain incorporated 3 future emission scenarios, 17 GCMs, and 3 scaling methods, generating an extensive ensemble of projections for the future period from 2041 to 2090. In total, 153 ensembles were utilized in our analysis. The modeling chain was applied individually to each grid and pooled the data from grids for a regional scaling. This study adapted the 26 regions from IPCC Special Report on Managing the Risks of Extreme Events and Disasters to Advance Climate Adaptation (SREX) (Seneviratne et al., 2012) (Fig. S1). Subsequently, the Sobol' sensitivity analysis (Sobol', 1990) was employed to determine the uncertainty contribution from each source. Moreover, Sobol' sensitivity analysis was systematically conducted across all possible combinations of GCMs to investigate how the number of GCMs influences their contribution to overall uncertainty

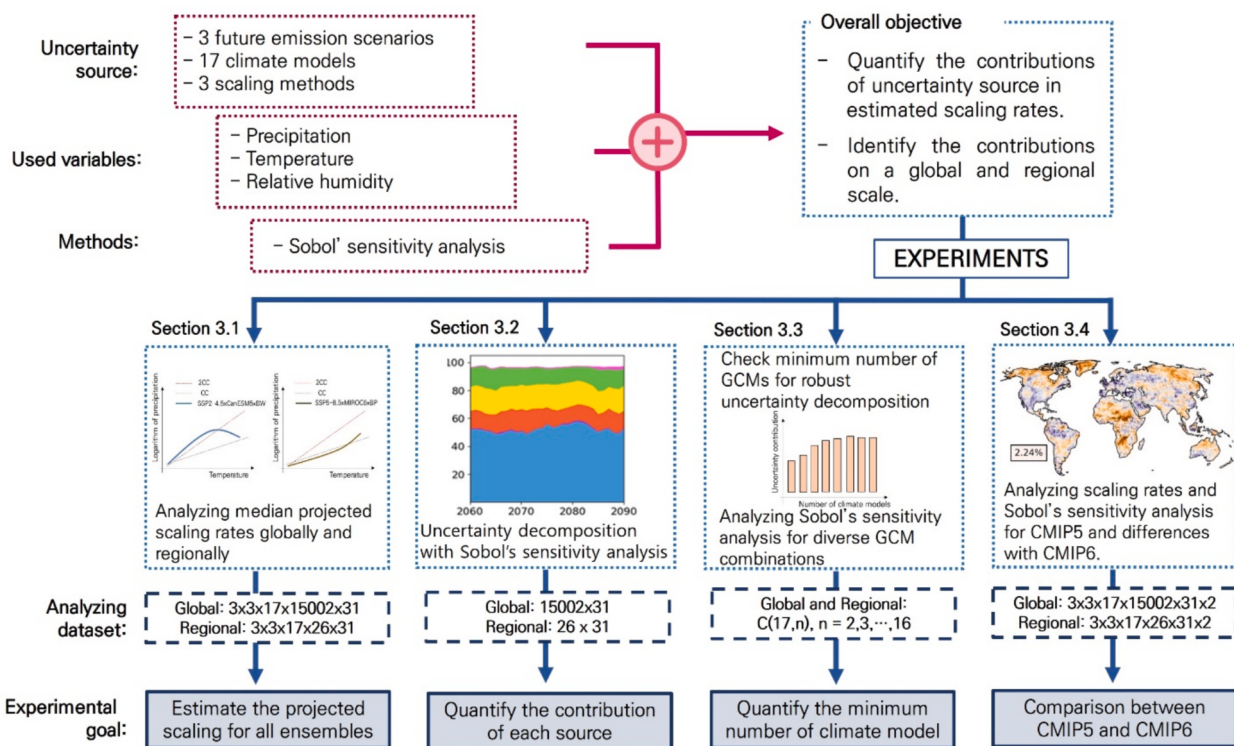


Fig. 1. The overview of the study design.

quantification.

2.1. Future emission scenarios

In this study, three future emission scenarios were selected: SSP1-2.6, SSP2-4.5, and SSP5-8.5, which represent low, medium, and high future emission levels, respectively (O'Neill et al., 2016). The SSP1-2.6 scenario represents a sustainability “taking a green road” with a radiative forcing of 2.6 W/m^2 , SSP2-4.5 denotes as a “middle of the road” scenario with a radiative forcing of 4.5 W/m^2 , and SSP5-8.5 portrays an “end of the road” scenario with a radiative forcing of 8.5 W/m^2 (Riahi et al., 2017). These three scenarios encompass a broad range of possible future emissions. Additionally, previous uncertainty decomposition studies, including Lehner et al. (2020), Wu et al. (2024) and Zhang et al. (2023) have also utilized these scenarios in their studies.

2.2. Global circulation models (GCMs)

The daily precipitation (Pr), surface air temperature (Tas), and near surface relative humidity ($Hurs$) were obtained from 17 GCMs, each developed by a different modeling institute, using the same initial realization (r1i1p1f1) (see Table 1). We aimed to include as many GCMs as possible; however, at the time of this study, only 17 GCMs provided daily data for all three variables. Additionally, we avoided using multiple GCMs from the same institute to prevent redundancy, as models from the same institute often have similar dynamic and physical parameterizations (Pathak et al., 2023), leading to comparable climate projections (Kuma et al., 2023). All variables obtained from GCMs were interpolated to $1^\circ \times 1^\circ$ resolution using the Inverse Distance Weighting (IDW) method prior to further analysis.

Based on Tas and $Hurs$, the dewpoint temperature ($Tdew$) was developed to serve as a scaling variable. This selection follows the recommendations of Van de Vyver et al. (2019), Wasko et al. (2018) and Zhang et al. (2019). In particular, Zhang et al. (2019) reported that for the response of extreme precipitation to rising temperatures across all three data sources (station-based, reanalysis, and climate model

Table 1
Summary of the seventeen CMIP6 GCMs utilized in this study.

Model	Resolution (lat \times lon)	Institution
ACCESS-CM2	$1.25^\circ \times 1.875^\circ$	Commonwealth Scientific and Industrial Research Organisation, Australia
AWI-CM-1-1-MR	$0.9375^\circ \times 0.9375^\circ$	Alfred Wegener Institute, Helmholtz Centre for Polar and Marine Research, Germany
CESM2-WACCM	$0.9375^\circ \times 1.25^\circ$	National Center for Atmospheric Research, USA
CMCC-ESM2	$0.9375^\circ \times 1.25^\circ$	Centro Euro-Mediterraneo sui Cambiamenti Climatici, Italy
CanESM5	$2.8^\circ \times 2.8^\circ$	Canadian Centre for Climate Modelling and Analysis, Canada
EC-Earth3	$0.7^\circ \times 0.7^\circ$	EC-EARTH consortium, The Netherlands/Ireland
FGOALS-g3	$2.25^\circ \times 2.0^\circ$	Chinese Academy of Sciences, China
GFDL-ESM4	$1.0^\circ \times 1.0^\circ$	NOAA Geophysical Fluid Dynamics Laboratory, USA
IITM-ESM	$1.9^\circ \times 1.875^\circ$	Centre for Climate Change Research, Indian Institute of Tropical Meteorology, India
INM-CM4-8	$1.5^\circ \times 2.0^\circ$	Institute for Numerical Mathematics, Russia
IPSL-CM6A-LR	$1.25^\circ \times 2.5^\circ$	Institut Pierre Simon Laplace, France
KACE-1-0-G	$1.25^\circ \times 1.875^\circ$	Nat. Inst. of Meteorological Sciences/Korea Meteorological Admin, South Korea
MIROC6	$1.4^\circ \times 1.4^\circ$	Japan Agency for Marine-Earth Science and Technology, Atmosphere and Ocean Research Institute, National Institute for Environmental Studies, Japan
MPI-ESM1-2-LR	$1.875^\circ \times 1.875^\circ$	Max Planck Institute for Meteorology, Germany
MRI-ESM2-0	$1.125^\circ \times 1.125^\circ$	Meteorological Research Institute, Japan
NorESM2-LM	$1.875^\circ \times 2.5^\circ$	Norwegian Climate Center Services, Norway
TaiESM1	$0.9375^\circ \times 1.25^\circ$	Taiwan Earth System Model, Taiwan

simulations), dewpoint temperature is a more realistic metric than surface air temperature, as it helps reduce the deviation of scaling rates from the expected CC scaling. To be specific, $Tdew$ was calculated by the

following formula (Alduchov and Eskridge, 1996):

$$Tdew = \frac{B \times \left(\left(\frac{A \times Tas}{B + Tas} \right) + \log \left(\frac{Hurs}{100} \right) \right)}{A - \left(\left(\frac{A \times Tas}{B + Tas} \right) + \log \left(\frac{Hurs}{100} \right) \right)} \quad (1)$$

where $A = 17.27$ and $B = 237.7$.

2.3. Scaling methods

The scaling rate between daily dewpoint temperature and wet-day precipitation (defined as days with precipitation higher than 0.1 mm/day) was estimated for each grid/region using three different scaling methods: binning with equal bin-width (BW), binning with equal sample data points (BP), and quantile regression (QR). These methods were applied across 31 simulation periods, each spanning 20 years. In other words, we utilized 20 years of continuous data from year $t-19$ to t (where t ranges from 2060 to 2090) to estimate the scaling rate for each grid/region. In our analysis, the 99th quantile was chosen as the extreme precipitation (PE) index for all three scaling methods. While other high quantiles of precipitation could be selected, we opted for the 99th quantile because it is commonly used in scaling rate estimation (Ali et al., 2018; Wang and Sun, 2022; Wasko and Sharma, 2014). However, the 95th quantile was also explored to confirm the robustness of our findings, and the results are provided in the [Supplementary Material](#).

For BW, we stratified the precipitation data by dewpoint temperature bins, each with a fixed width of $\sim 2^{\circ}\text{C}$ (defined as 2°C in this study). In each bin, we selected a pair of PE and average dewpoint temperature (\widehat{Tdew}). Afterwards, the series of $PE - \widehat{Tdew}$ pairs obtained from all bins were fitted to a linear regression model, denoted as:

$$\log(PE) = \beta_0 + \beta_1 \widehat{Tdew} \quad (2)$$

The scaling rate (α_t) of each simulation period from $t-19$ to t was then obtained by using exponential transformation of the slope coefficient of the model (β_1), as shown in Eq. (3).

$$\alpha_t = 100 \times (\exp(\beta_1) - 1) \quad (3)$$

For the second method, BP, the methodology began by categorizing precipitation data based on dewpoint temperature into ℓ equal bins (30 bins used in this study), ensuring each bin contained an equal amount of precipitation data. Subsequently, PE and their corresponding $Tdew$ were selected in each bin. To analyze the relationship between PE and \widehat{Tdew} , we applied locally weighted regression (LOWESS) smoothing (Cleveland, 1979) to the $PE - \widehat{Tdew}$ pairs. LOWESS, recognized for its ability to identify peak-points in scaling with hook-shaped structures, was chosen based on its application in previous studies (Gu et al., 2023; Utsumi et al., 2011). Following the approach outlined by Utsumi et al. (2011), we applied smoothed PE against \widehat{Tdew} before peak-point for the hook-shaped relationships, and across entire series for monotonic relationships. This fitting was performed using a linear model described by Eq. (2), and subsequently, the scaling rate was estimated based on Eq. (3).

Different from the previous two scaling methods, in QR, we fitted the logarithm of PE and $Tdew$ to a linear model based on a conditional quantile. While linear regression considers only the mean of the response variable, QR focuses on a specific quantile of interest (Wasko and Sharma, 2014). The fitting of QR between logarithm of precipitation and dewpoint temperature at q th quantile can be expressed as:

$$\log(PE) = \beta_0^q + \beta_1^q Tdew \quad (4)$$

The scaling rate for QR was estimated by the exponential transformation of the slope coefficient (β_1^q) using Eq. (3).

2.4. Framework for decomposing uncertainty in scaling rate projections

The uncertainty of the scaling rates was decomposed into contributions from different sources using Sobol' sensitivity analysis. Similar to the factorial experimental design of Analysis of Variance (ANOVA), Sobol' sensitivity analysis aims to decompose the variance of model output. However, Sobol' sensitivity analysis is advantageous because it can handle nonlinear relationships (Archer et al., 1997). Moreover, Sobol' sensitivity analysis quantifies the uncertainty contributions from individual sources as well as the higher-order interactions among these sources.

To clarify, if α_t is an ensemble of scaling rate for the period from $t-19$ to t with total of 153 estimated values, the total variance of α_t can be decomposed to different components, as shown below:

$$V(\alpha_t) = \sum_i V_i + \sum_i \sum_{j>i} V_{ij} + V_{123} \quad (5)$$

where $V(\alpha_t)$ is total variance of estimated scaling rates α_t at the t -year-based period. V_i is variance contribution from main sources (future emission scenarios, GCMs and scaling methods), V_{ij} is variance contribution from the interaction between two main sources (future emission scenarios and GCMs, future emission scenario and scaling method, and GCMs and scaling methods), and V_{123} is variance contribution from three main sources.

The sensitivity indices (S) was used to describe how each component contributes to the total variance. It was calculated by dividing both sides of Eq. (5) by $V(\alpha_t)$, as shown:

$$\sum_i S_i + \sum_i \sum_{j>i} S_{ij} + S_{123} = 1 \quad (6)$$

Here, S_i , S_{ij} , S_{123} , are the sensitivity indices for the three individual main sources, interaction between two main sources, and interaction between all three main sources, respectively. If a component with higher sensitivity indices, indicating that it contributes more to the total uncertainty. For a detailed explanation of how $V(\alpha_t)$ is partitioned and how sensitivity indices are computed, refer to Saltelli et al. (2010).

2.5. GCMs Quantity in uncertainty decomposition framework

GCMs are generally shown to be the primary contributors to the overall uncertainty in the uncertainty decomposition studies (e.g., Ji et al., 2024; Lehner et al., 2020; Wu et al., 2024). Using a small number of GCMs may underestimate the contribution from GCMs (Wang et al., 2020), but using too many GCMs requires more time and may cause computational burden. Hence, it is important to quantify an appropriate amount of GCMs. Here, our objective was to ascertain the optimal number of GCMs for the scaling rate uncertainty decomposition framework, with implications for future reference.

To achieve this goal, we employed the Sobol' sensitivity analysis across all possible combination of GCMs, exploring subset sizes ranging from 2 to 16 GCMs. This approach allowed us to systematically evaluate how each number of GCMs determine the uncertainty contribution to the overall uncertainty. Instead of arbitrarily selecting samples for each subset, this study calculated the average for every possible combination of GCMs, similar to the approach utilized in Wang et al. (2020) and Zhang et al. (2023). For example, starting with a subset of 2 GCMs, we conducted the Sobol' sensitivity analysis on a total of $C(17, 2) = 136$ unique pairs of models. The obtained uncertainty contribution from each number of GCMs were then compared to the contribution from full set of GCMs to identify an optimal number of GCMs. Subsets that exhibited uncertainty contributions comparable to those of the full set of GCMs were considered better subsets in this context.

3. Results

3.1. Projected scaling rates and their variations

We begin our analysis by estimating the scaling rate for all ensembles, both globally and regionally, using different scenarios and scaling methods. Fig. 2 depicts the global distribution of scaling rates across simulation periods, along with the corresponding trends in PE and T_{dew} . The results indicate that the median estimated scaling rates among the 17 GCMs range from approximately $-1\%/\text{C}$ to about $1.5\%/\text{C}$. Furthermore, most estimated scaling rates tend to decrease over time, possibly due to the significant increase in T_{dew} compared to PE (see Fig. 2b).

As shown in Fig. S2, the scaling rates vary by region, encompassing both negative and positive values, with negative scaling observed in half of all regions. This regional disagreement leads to lower global scaling. Moreover, in both global and regional scaling, the line plots reveal a clear pattern, where scaling methods are grouped together, while each group also shows distinct variation across future emission scenarios. Throughout all simulation periods, the BW estimates the highest scaling rates, followed by the QR, while the BP returns the lowest scaling rates.

It is also observed that SSP1-2.6 consistently estimates the highest scaling rates over time, while SSP5-8.5 projects the lowest scaling rates with a small reduction in the far future. The trends in projected scaling rates under SSP5-8.5 demonstrate a significant decrease across all three scaling methods. This variation may also be explained by the trends of PE and T_{dew} shown in Fig. 2b, where both variables increase over time, though the rate of increase depends on the future emission scenario. In SSP1-2.6, both PE and T_{dew} exhibit minimal increases at a similar rate, as indicated by the nearly parallel trend lines. In contrast, in SSP2-4.5 and particularly SSP5-8.5, the increases in PE and T_{dew} diverge. T_{dew} shows high sensitivity to future emission scenarios, leading to a more pronounced increase, especially in the far future. This analysis suggests that both the choice of scaling methods and future emission scenarios may affect scaling rate estimation, further highlighting the need to quantify their contribution to scaling rate projections.

3.2. Uncertainty decomposition of the projected scaling rates

Next, we present the average and spread (difference between the 90th and 10th quantiles) across all ensembles for each grid and region over the entire simulation period (2041–2090) to illustrate the spatial

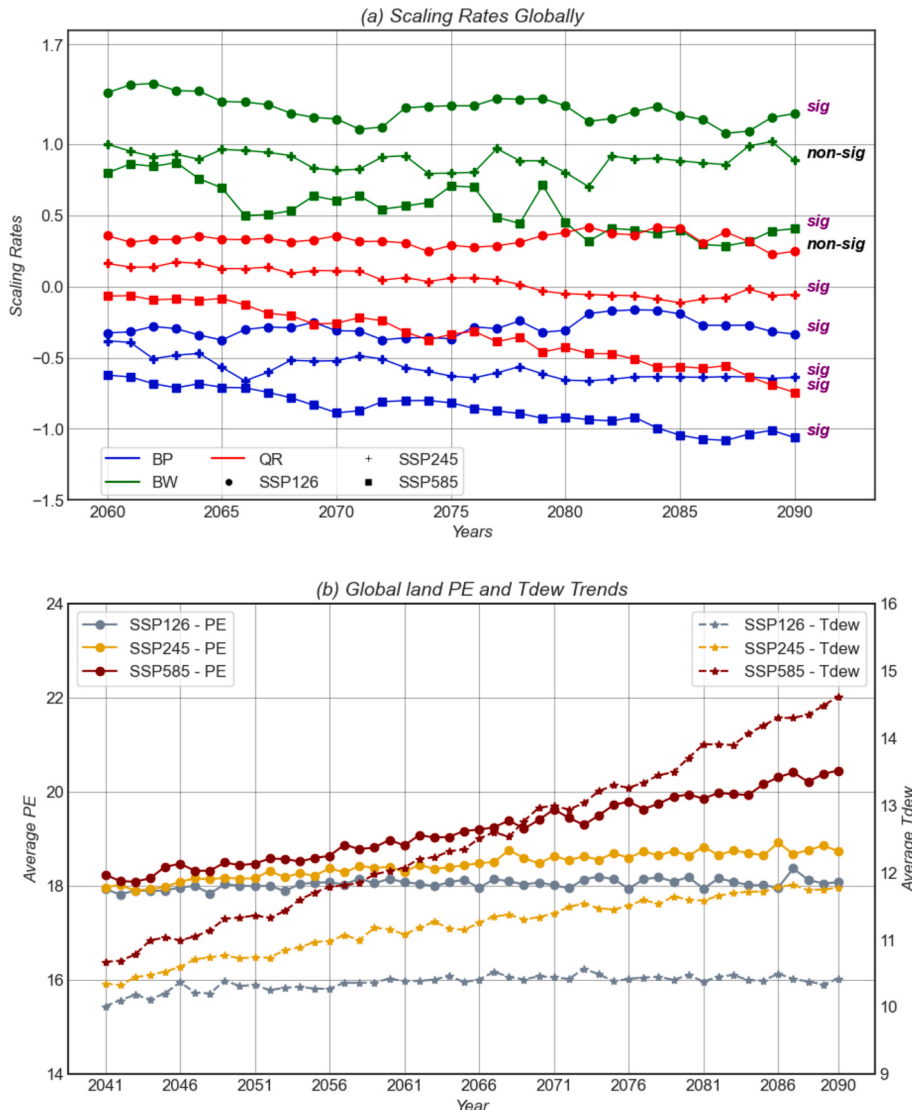


Fig. 2. (a) Median projected scaling rates from 17 GCMs across various scenarios and scaling methods, with distinct colors indicating different scaling methods and marker shapes representing future emission scenarios. The text at the end of each line denotes the significance of the trend regressed over time. (b) Annual trends in Average PE averaged over global land, with colors indicating different scenarios and circle markers representing PE and star markers representing T_{dew} .

distribution of the estimated scaling rates (Fig. 3). Several insights emerge from this figure. Firstly, the scaling rates show considerable variability, ranging from $-30\text{ \textperdegree C}$ to over $10\text{ \textperdegree C}$ when analyze on a grid-by-grid-based (see Fig. 3a). Negative scaling rates are particularly notable in the intertropical belt at low latitudes, spanning from northern Australia and Southeast Asia to southern India, central Africa, and Brazil in South America. The lowest scaling rate is observed along the coastal areas of the Brazilian Amazon. Moving towards higher latitudes, higher scaling rates are observed, including ALA and EAS. Moreover, when considering regional scaling rates, the variability tends to decrease, reflecting a more realistic scenario (Fig. 3b). Specifically, the scaling rate ranges from $-10\text{ \textperdegree C}$ to approximately $3\text{ \textperdegree C}$, showing similar spatial patterns as the individual grid scaling rates. In the regional analysis, the CGI region exhibits the highest scaling rate, followed by ALA, EAS, NEU, NAS, and SSA. Conversely, regions located in the intertropical belt such as SEA, EAF, WAF, AMZ, and particularly NEB show the lowest scaling rates. Regional differences in scaling rates can be partly explained by variations in moisture availability (Barbero et al., 2018; Hardwick Jones et al., 2010). Some regions have sufficient moisture to support increased evaporation and precipitation, while others experience moisture limitations despite rising temperatures. Lastly, a diverse range of grid and regional scaling rates across the ensemble is observed (see Fig. 3c and d). In both analyses, areas within the intertropical belt that demonstrates low scaling rates also exhibit considerable variability among the 153 ensembles, likely due to the geographical complexity and the fact that this area is a subsidence zone of Hadley cells, which may affect the performance of GCM simulations. In contrast, higher latitudes generally showed less variability.

Given the high spread of the estimated scaling rates, we decompose them into contributions from different sources within the modeling chain. Fig. 4 represents the uncertainty contribution from different sources for each grid throughout the entire simulation period. Specifically, Fig. 4a–c illustrate the uncertainty contribution from three main

sources, while Fig. 4e–f show the interactions between two main sources. The values displayed in the box at the bottom left of each panel represent the global averages. GCMs are the primary contributor to the overall uncertainty across most regions worldwide, with the highest contribution observed in areas with geographical complexity such as the Tibetan Plateau of China. This leads to a high global average contribution of 40.38 % to the overall uncertainty from GCMs. The scaling method plays the second most significant role, contributing an average of 13.71 % globally to the overall uncertainty. High contributions from both sources also result in a somewhat elevated contribution from the interaction between GCMs and scaling methods, averaging 17.37 % globally. In contrast, future emission scenarios contribute minimally, with a global average of only 2.70 %, suggesting that the choice of future emission scenarios may have relatively less impact on future projections.

Subsequently, we examine the uncertainty contribution from each source to the overall uncertainty across all regions and simulation periods. Fig. 5 displays 6 out of 26 regions along with the global average, while the remaining 20 regions are illustrated in Fig. S3. Generally, GCMs are the predominant source of uncertainty throughout all simulation periods, except for AMZ, NAS, NEB, SAU, and WAF, where scaling methods have a greater contribution. EAS shows the highest contribution from GCMs and the lowest from scaling methods, averaging 68.32 % from GCMs and 0.85 % from scaling methods over the simulation periods. Conversely, WAF exhibits the lowest contribution from GCMs at 27.59 %, whereas SAU has the highest contribution from scaling methods, averaging 51.13 %. Future emission scenarios contribute minimally to the uncertainty from scaling rates across all regions but have a more notable effect when interacting with GCMs. The interaction between the GCMs and scaling methods also contributes significantly in some regions. Specifically, in regions like MED, SAS, and CEU, it contributes almost 30 %. This suggests that when estimating scaling rates, it is important to consider multiple scaling methods, as their interaction with GCMs is non-linear, and relying on just one method could lead to

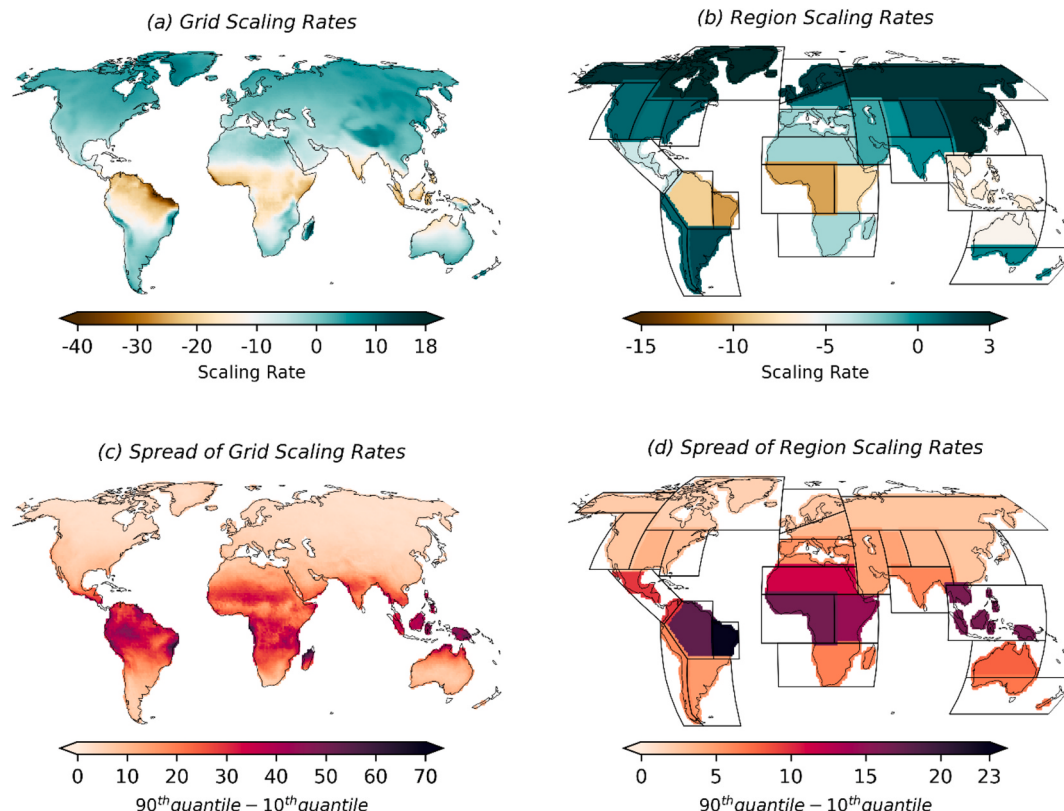


Fig. 3. The average of estimated scaling rates and their spread (difference between the 90th and 10th percentiles) across 153 ensembles for the entire simulation period (2041–2090): (a) average scaling rate for grids, (b) average scaling rate for regions, (c) spread for grids, and (d) spread for regions.

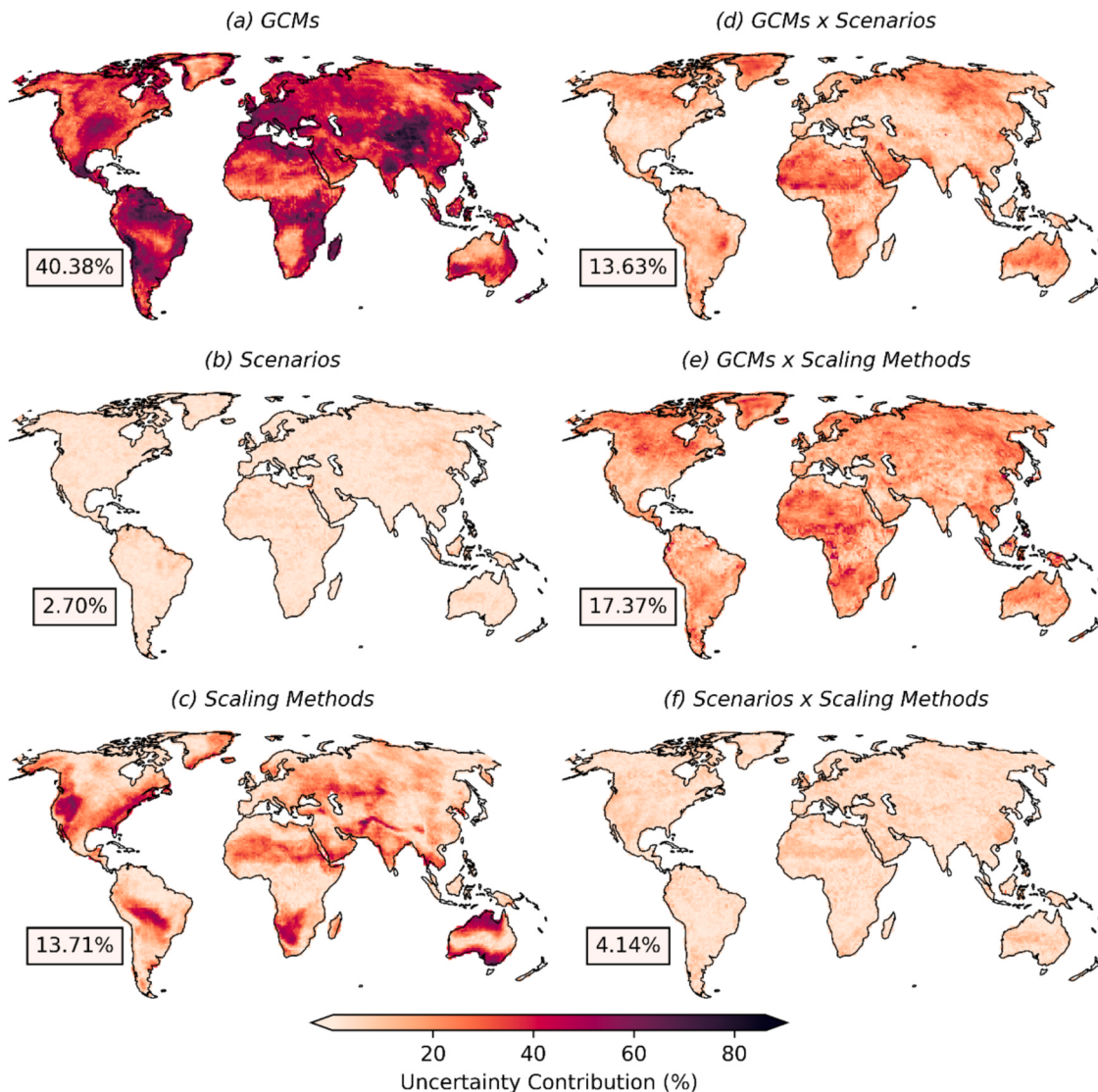


Fig. 4. Global uncertainty contributions from each .

Source: (a) GCMs, (b) future emission scenarios, (c) scaling methods, (d) interaction between GCMs and future emission scenarios, (e) interaction between GCMs and scaling methods, and (f) interaction between future emission scenarios and scaling methods. The values in the box at the bottom left of each panel represent the global average across all grid points

misinterpretation of the results. Upon reviewing the temporal changes in uncertainty contributions, we found that the contribution from all sources remained relatively stable across all 31 simulation periods for all regions, with only minor variations. Notably, the contribution from future emission scenarios increases in the far future for certain regions, such as NAU, CEU, CNA, TIB, and SAU. The contribution from scaling methods remains consistent through most simulation periods, though they decrease over time in regions like WAF, WSA, and CEU, while showing an increasing trend in regions such as SAF, NAU, SSA, and SAH. GCMs also exhibit minimal variation, generally decreasing in regions like WNA, SEA, SAH, and CEU. However, it is worth noting that the changes in contribution from all sources are minor, leading to a stable global average, as depicted in Fig. 5g. On a global scale, GCMs consistently account for the highest uncertainty contribution at 46.82 %, followed by scaling methods at 23.75 %, and the interaction between GCMs and scaling methods at 19.83 %. Future emission scenarios, along with their interactions with GCMs and scaling methods, contribute modestly to the overall uncertainty.

3.3. GCM quantity in the uncertainty decomposition framework

GCMs are the major source of the uncertainty of estimated scaling rates in most regions, as noted in the previous section. Here, we explore the optimal number of GCMs required to achieve robust results within this uncertainty decomposition framework. Fig. 6 displays the uncertainty contribution from GCMs, averaging all possible combinations of GCMs (ranging from 2 to 17) across all simulation periods for 6 regions and globally for all the simulation periods. The other 20 regions are shown in Fig. S4. From Figs. 6a and S4, it is observed that with a low number of GCMs, the framework underestimates the uncertainty contribution from GCMs. However, as the number of GCMs increases, their contribution to the uncertainty also increases across all regions. Generally, when the number of GCMs is increased to 8 or 9, their contribution to the uncertainty starts to approach the $\pm 5\%$ range of uncertainty contribution from 17 GCMs. To be specific, the framework requires at least 8 or 9 GCMs to be robust for 22 out of 26 regions. However, for the remaining four regions, additional GCMs are required: the framework needs at least 11 GCMs for NAS, 10 for SAF, and 14 each for both ALA and WSA. For the global average, similar interpretation can

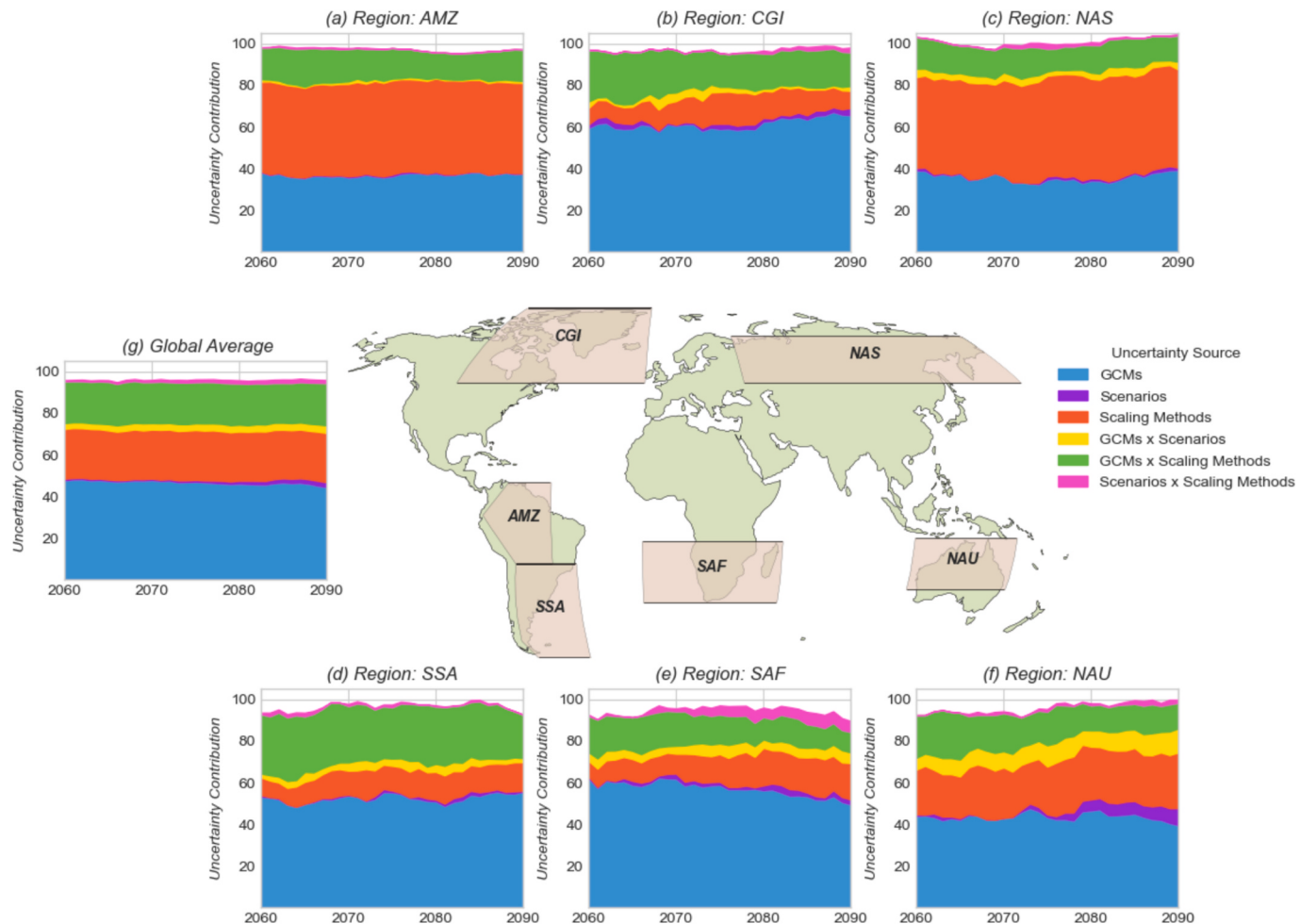


Fig. 5. Uncertainty contribution from all sources for six SREX regions: (a) AMZ, (b) CGI, (c) NAS, (d) SSA, (e) SAF, and (f) NAU; along with (g) the global average. In each panel, colors represent the uncertainty contribution from different sources: blue for GCMs, purple for future emission scenarios, red for scaling methods, yellow for interactions between GCMs and future emission scenarios, green for interactions between GCMs and scaling methods, and pink for interactions between future emission scenarios and scaling methods. The remaining white space illustrates the interactions among all three primary sources. (For interpretation of the references to color in this figure legend, the reader is referred to the web version of this article.)

be found. In all simulation periods, the contribution from GCMs increases with the number of GCMs utilized. Using only 2, 3, or 4 GCMs results in a notably low contribution. When 9 GCMs are used, the uncertainty contribution from GCMs falls in the $\pm 5\%$ range of the 17 GCMs for all the simulation periods. For GCM counts from 9 to 16, the uncertainty contribution consistently falls within this range. Specifically, the average difference in uncertainty contribution between using 17 GCMs and 2 GCMs is 20.61 %, while the difference between using 17 GCMs and 9 GCMs is only about 1.71 %.

Next, we investigate the impact of the number of GCMs on other sources of uncertainty by selecting sample combinations for each possible number of GCMs used. The sample selection approach is as follows: First, we group all combinations of each number of GCMs based on the individual GCMs contained within those combinations. Each group corresponds to combinations that share a common GCM. Then, from each group, we randomly select one combination. This process ensures that for each number of GCMs, we obtain 17 samples (one from each group corresponding to each GCM). For example, when the number of GCMs is 2, the first group will contain combinations such as (ACCESS-CM2, AWI-CM-1-1-MR), (ACCESS-CM2, CESM2-WACCM), and so on. Within this group, we randomly select one sample. We repeat this process for all other 16 groups. This approach allows us to explore the uncertainty contribution more comprehensively across different numbers of GCMs, by capturing a representative subset of combinations

without biasing the results toward certain combinations. Fig. 7 illustrates the distribution of sampled combinations for seven different GCM sample sizes (2, 5, 9, 10, 12, 14, 16) across six regions, as shown in Figs. 5 and 6. The remaining 20 regions are presented in Fig. S5. The results indicate that for all regions, a low number of GCMs (e.g., 2, 5) leads to significant disagreement among the combinations. For example, in the NAU region, using only 2 GCMs results in high variability, with some combinations indicating that GCMs are the largest source of uncertainty, while others suggest that scaling methods dominate. This variability highlights that with fewer GCMs, the contribution of GCMs to overall uncertainty is underestimated, leading to an overestimation of the uncertainty attributed to scaling methods. Additionally, the contribution from future emission scenarios and their interaction with scaling methods is also exaggerated under low GCM conditions. However, as the number of GCMs increases, the agreement among combinations improves, especially from 9 GCMs onward, where most regions exhibit consistent uncertainty distribution patterns. Therefore, when decomposing the uncertainty of scaling rates for extreme precipitation using CMIP6 data, researchers should consider using a sufficient number of climate models, with at least 9 GCMs recommended.

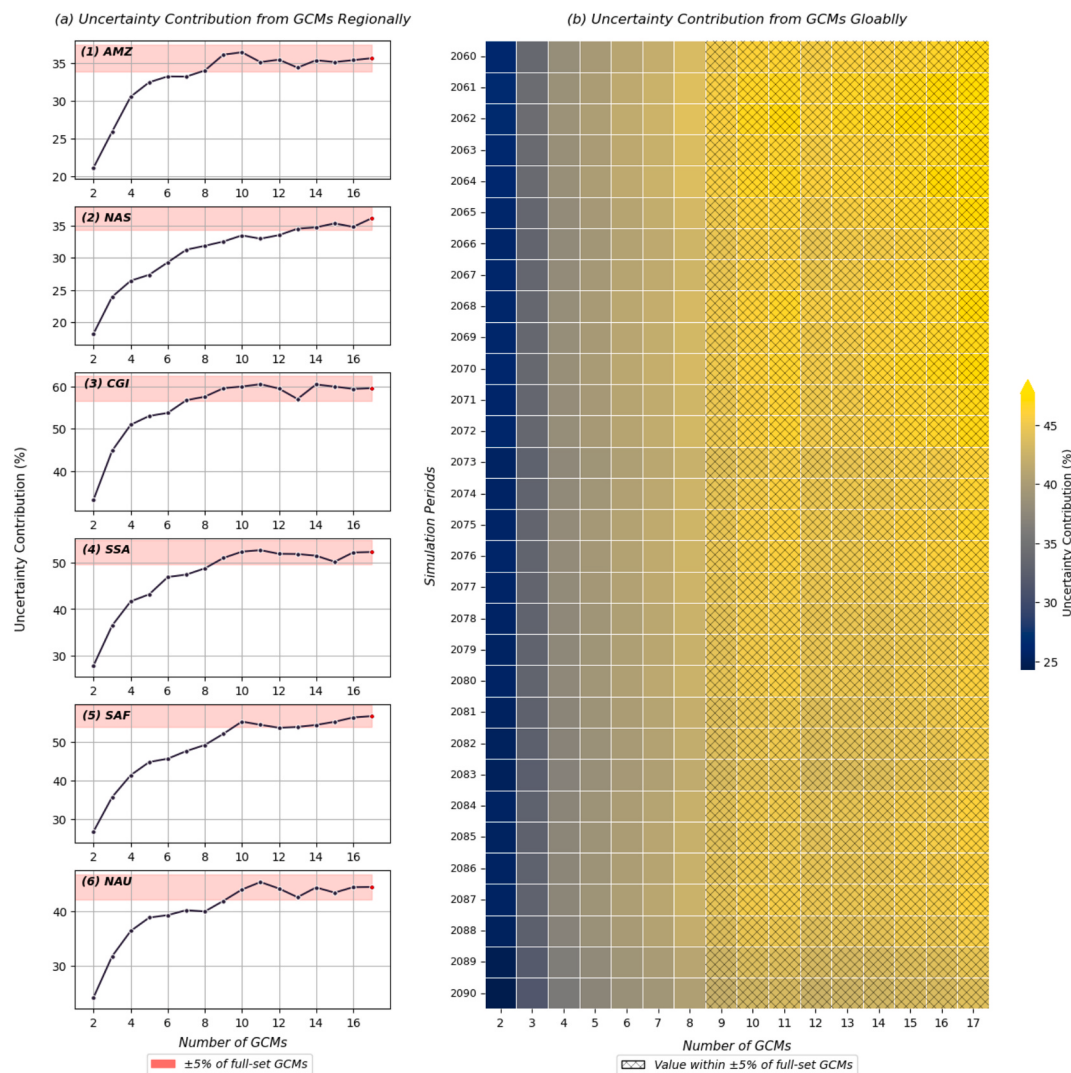


Fig. 6. Uncertainty contribution from varying numbers of GCMs, ranging from 2 to 17. (a) Average uncertainty contribution over 31 simulation periods from GCMs of 6 regions that were presented in Fig. 4. Each scatter point represents the average values of all possible combination pairs taken from the 17 GCMs. The shaded red line denotes the $\pm 5\%$ of uncertainty contribution from the 17 GCMs, represented by red points. (b) Globally averaged uncertainty for each simulation period. The hatch in each cell of the heat map indicates values within $\pm 5\%$ of uncertainty contribution from the 17 GCMs. (For interpretation of the references to color in this figure legend, the reader is referred to the web version of this article.)

3.4. Uncertainty decomposition of CMIP5 scaling rates and the comparison with CMIP6

In this section, we analyze data from CMIP5 and compare it with CMIP6 to evaluate the differences in the contribution of each uncertainty source to overall uncertainty. Based on the findings from the previous section, where it was determined that at least 9 GCMs are necessary for a robust uncertainty decomposition, we use 10 GCMs from CMIP5. These GCMs are analyzed across three future emission scenarios—RCP26, RCP45, and RCP85—representing low, medium, and high greenhouse gas emissions, respectively. Detailed information on the selected 10 GCMs is provided in Table S1. In Fig. S6, we recreate Fig. 3 to compare the differences between estimated scaling rates globally and regionally, both in terms of the average and the spread among the 90 ensembles. The results indicate that the average scaling rates and their spread exhibit a similar spatial distribution globally similar to those in CMIP6. Negative scaling rates are observed in the intertropical belt, with the lowest values along the coastal areas of the Brazilian Amazon, while higher scaling rates are prevalent in higher latitude regions. However, it is important to note that in CMIP5, the maximum spread is greater than in CMIP6, highlighting significant variability between the ensembles.

Regionally, the estimated scaling rates show similar spatial patterns, with the lowest values in WAF and the highest spread consistent with CMIP6 observed in NEB and SEA.

To understand the spatial distribution of uncertainty contributions from all sources in CMIP5, we decompose the uncertainty in scaling rates across the 90 ensembles and recreate Fig. 4, as illustrated in Fig. S7. The results show that the spatial distribution of uncertainty contributions in CMIP5 is similar to that in CMIP6. Specifically, GCMs contribute to the overall uncertainty the most at 44.95 %, while scaling methods and their interaction with GCMs contribute 17.26 % and 15.11 %, respectively. Future emission scenarios contribute a relatively low 3.04 %, which is higher than their interaction with scaling methods (2.83 %) but lower than their interaction with GCMs (11.36 %). Fig. 8 compares the uncertainty contributions from each source between CMIP6 and CMIP5, showing the differences (CMIP6 – CMIP5). The results indicate that the largest difference is in the contributions from GCMs, with CMIP5 GCMs contributing 4.57 % more globally than those in CMIP6. Spatially, CMIP5 shows higher contributions in regions such as central to northern Australia, northeast China to southeast Russia, southern and central Africa, and Canada. Conversely, GCMs from CMIP6 contribute more in regions like Brazil, India, the Middle East, and Europe. Future

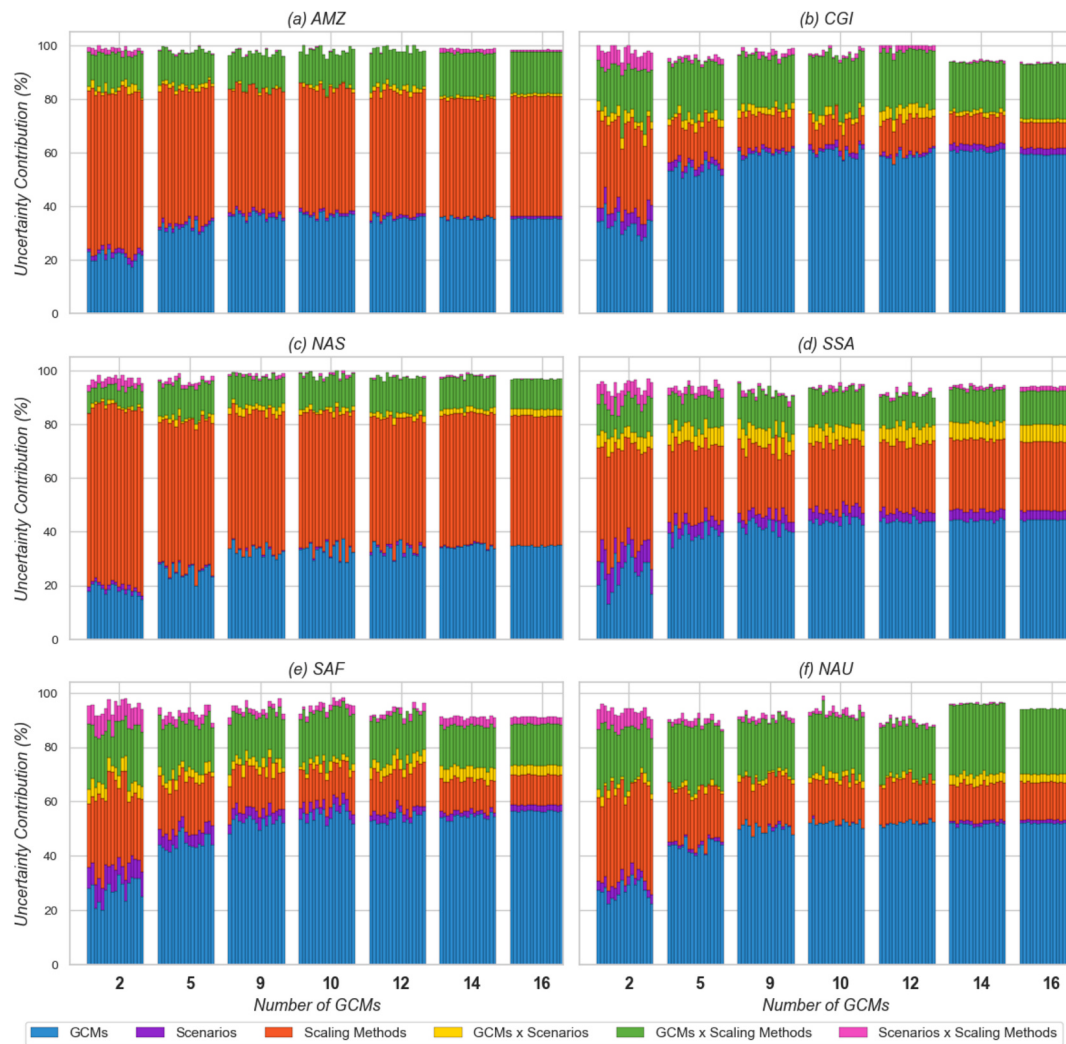


Fig. 7. Distribution of uncertainty contributions across six regions: (a) AMZ, (b) CGI, (c) NAS, (d) SSA, (e) SAF, and (f) NAU for different numbers of GCMs (2, 5, 9, 10, 12, 14, 16): Each bar represents a sample from combinations within each group of each number of GCM.

emission scenarios show the smallest difference between the two CMIP phases, with a global average difference of 0.75 %, where CMIP5 has a slightly higher contribution. For scaling methods, CMIP5 exhibits a global average difference of 3.72 %, indicating a higher contribution compared to CMIP6. This increased contribution is particularly evident in regions such as the southern Middle East, northern Africa, Greenland, Alaska, and the northeastern USA and Europe. Notably, all three main sources contribute more globally in CMIP5 than in CMIP6. However, interactions between these sources contribute more in CMIP6 compared to CMIP5. Specifically, interactions between GCMs and future emission scenarios, GCMs and scaling methods, and future emission scenarios and scaling methods in CMIP6 show greater contributions in most parts of the world, with global averages of 2.29 % and 2.24 %, respectively.

Fig. S8 presents the uncertainty decomposition of estimated scaling rates across each simulation period for all regions using CMIP5 data. The results indicate that GCMs are the highest contributors in most regions, except for AMZ, ENA, NAS, and SAU, where scaling methods contribute more, and NEU and WSA, where the interaction between GCMs and scaling methods has a higher contribution. Future emission scenarios contribute very little to overall uncertainty in all regions. Temporal changes are also found here, particularly for future emission scenarios, which show an increase over time in regions such as CEU, CGI, EAS, ENA, NAS, NEU, TIB, and WNA. For GCMs, the temporal changes vary by region. In CAM, SSA, and WNA, the contribution from GCMs

decreases slightly around 2080 but increases again after 2085. Conversely, the contributions from GCMs tend to decrease in regions like ALA, CGI, EAS, WNA, NAS, and WAF, while increasing in CEU, MED, SAF, and SAU. It should be highlighted that in CMIP5, the interaction between main sources contribute more than in CMIP6, notably the interaction between GCMs and future emission scenarios as well as GCMs and scaling methods.

The differences in uncertainty contributions from each source between CMIP6 and CMIP5 are presented in Fig. 9. The first column displays regional differences, and the second column shows the globally averaged differences for each simulation period. For the regional differences, it is observed that the differences between CMIP6 and CMIP5 are significant for GCMs and scaling methods. The average difference for GCMs reaches as high as 30 % in NAS and drops to -20 % in WNA and TIB. For scaling methods, the differences exceed -20 % in AMZ, ENA, and NAS and reach 20 % in EAS and NEU. The interactions between GCMs with scaling methods and future emission scenarios also show considerable differences between the two phases of CMIP. For example, in CGI, the difference exceeds -20 % for the interaction between GCMs and future emission scenarios, while in WSA, it reaches -20 % for the interaction between GCMs and scaling methods. Future emission scenarios and their interaction with scaling methods exhibit minimal differences between CMIP6 and CMIP5, with the highest difference for future emission scenarios being -10 % in CGI, and the interaction with

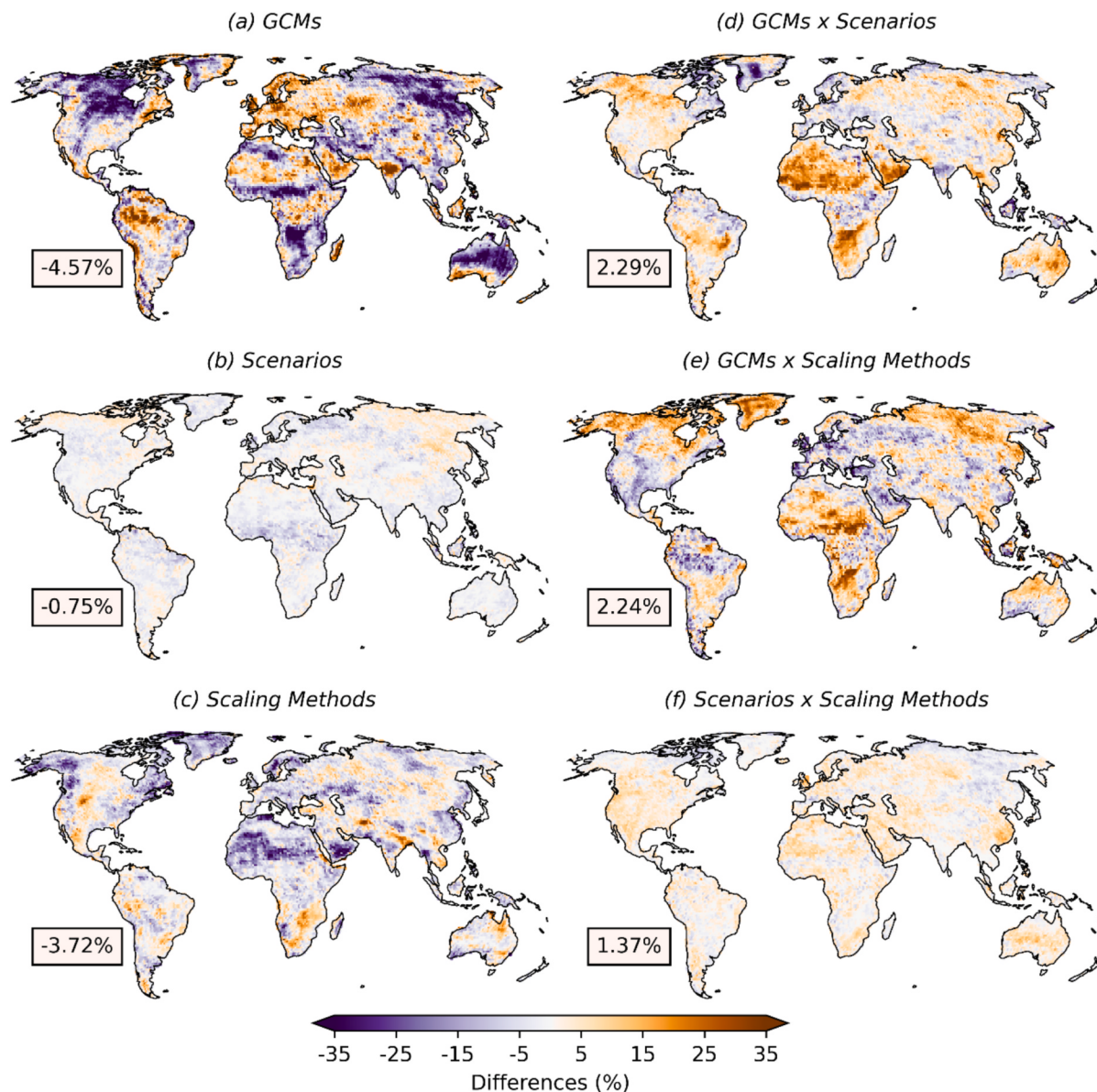


Fig. 8. The differences of the uncertainty contribution of each source between CMIP6 and CMIP5 (CMIP6-CMIP5). (a) GCMs, (b) future emission scenarios, (c) scaling methods, (d) interaction between GCMs and future emission scenarios, (e) interaction between GCMs and scaling methods, and (f) interaction between future emission scenarios and scaling methods. Purple color indicates negative values, where an uncertainty source contributes in CMIP5 more than in CMIP6, while orange indicates the opposite. The values in the box at the bottom left of each panel represent the global average across all grid points. (For interpretation of the references to color in this figure legend, the reader is referred to the web version of this article.)

scaling methods shows differences around 1 % to -1%. To be specific, CMIP6 has higher contributions to the overall uncertainty than CMIP5 in 12 out of 26 regions for GCMs, 19 regions for future emission scenarios, 16 regions for scaling methods, 9 regions for the interaction between GCMs and future emission scenarios, 8 regions for the interaction between GCMs and scaling methods, and 23 regions for the interaction between future emission scenarios and scaling methods. From the global averaged perspective in each simulation period, the differences are not significant in all simulation periods for the GCMs. However, the spread is huge, ranging from -20 % to 20 %. While for future emission scenarios, the difference is found, but not a huge percentage. The differences in future emission scenarios in CMIP6 contribute more than in CMIP5 before 2076 but turn lower than in CMIP5 after 2080, while for the differences in the scaling methods, it is found that in CMIP6 is higher than in CMIP5 in all simulation periods. For the interactions between main sources, interaction between GCMs and future emission scenarios contribute less in CMIP6 than in CMIP5 in all simulation periods, while

future emission scenarios and scaling methods contribute more in CMIP6 than in CMIP5. Interaction between GCMs and scaling methods shows no significant differences.

4. Discussion

In this study, we showed that GCMs are the primary contributor to the overall uncertainty across most regions worldwide in the uncertainty of scaling rates. However, since the choice of extreme precipitation index can affect scaling rate estimation (Pumo et al., 2019), we further examined uncertainty contributions using the 95th quantile to test the robustness of our findings. Fig. S9 shows the uncertainty contributions from each source globally, based on the 95th quantile. Fig. S10 illustrates regional scaling rate uncertainty decomposition across all simulation periods, while Fig. S11 presents the uncertainty contributions from GCMs for different numbers of GCMs across all regions. The analyses conducted using the 95th quantile show results that are generally

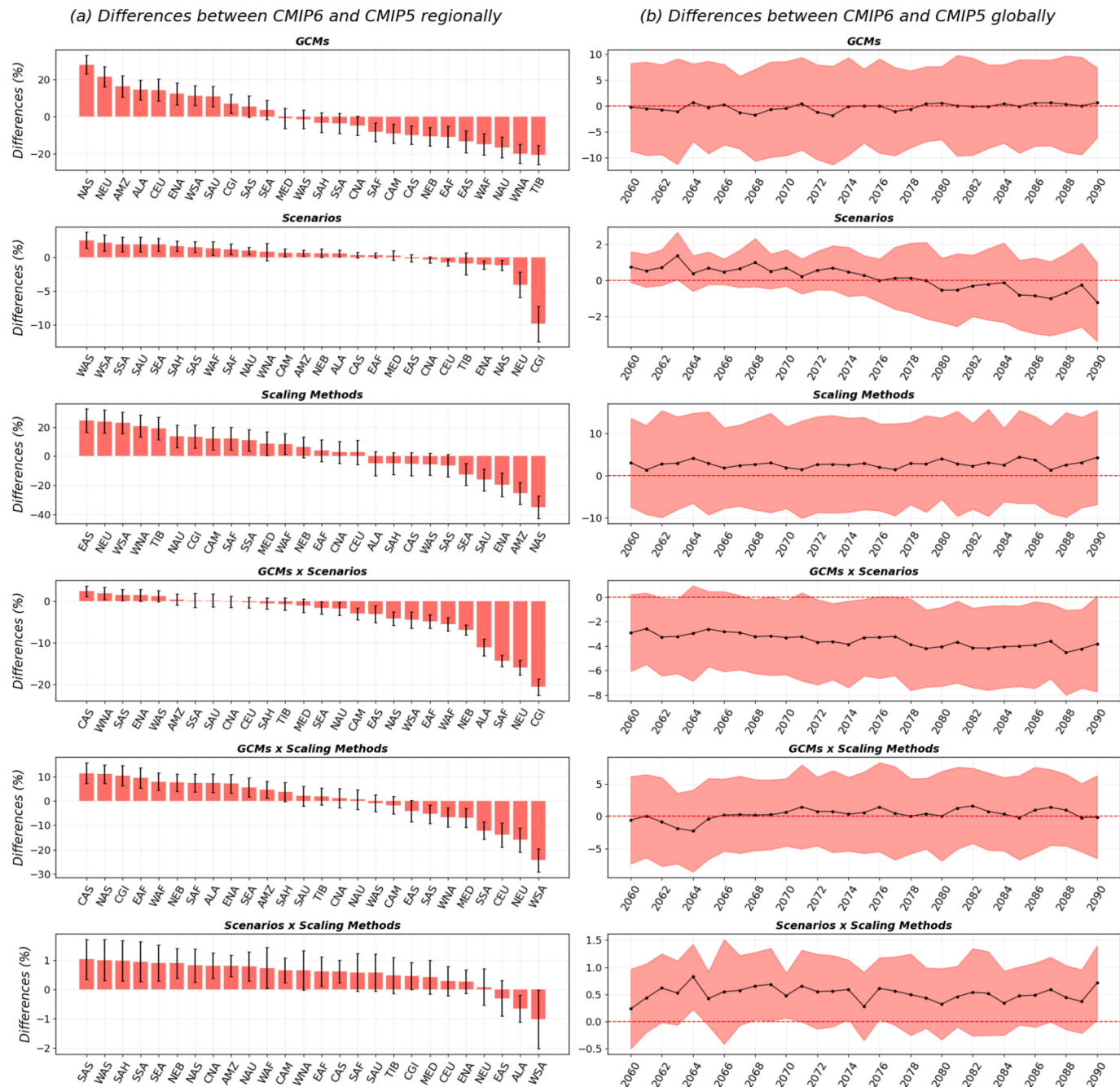


Fig. 9. Differences in uncertainty contributions between CMIP6 and CMIP5 (CMIP6 – CMIP5). The first column illustrates regional differences, with bars indicating the average across all simulation periods and error bars representing the magnitude of the standard deviation. The second column depicts global averages for each simulation period, with a line plot showing the average value and a shaded red area indicating the magnitude of the standard deviation. (For interpretation of the references to color in this figure legend, the reader is referred to the web version of this article.)

consistent with our main analysis, with only minor differences observed in some grids and regions. For instance, when uncertainty is decomposed on a grid-based, the spatial patterns remain similar, though GCM contributions are about 2 % higher than at the 99th quantile. Notably, the influence of scaling methods is slightly lower at the 95th quantile, while the contribution from future emission scenarios is higher. Differences in regional scaling rate uncertainty between the 95th and 99th quantiles are also minimal, with GCMs being the predominant source of uncertainty in most regions. However, in 14 out of 26 regions, the contribution from scaling methods is slightly lower than at the 99th quantile, with the most significant difference observed in NAU, where it exceeds 13 %. In over half of the regions, as well as in grid-based

decomposition, scaling methods contribute less to uncertainty at the 95th quantile compared to the 99th quantile. This suggests that using the 95th quantile may reduce methodological disagreement for determining the scaling rate. When determining the optimal number of GCMs for uncertainty decomposition using the 95th quantile, Fig. S11 reveals no significant difference from the recommendation of at least nine GCMs in most regions. Overall, while there are small variations, this additional analysis supports our conclusions.

Many studies about uncertainty decomposition for future climate projection have been conducted for different climate variables. This study contributes to this field by decomposing the uncertainty of scaling rates of extreme precipitation. Despite focusing on different climate

variables, our findings are largely consistent with previous studies, showing only slight deviations. For instance, similar to past studies (Ji et al., 2024; Lehner et al., 2020; Wu et al., 2024; Zhang et al., 2023), our analyses show that GCMs are the biggest contributor to the overall uncertainty. However, future emission scenarios, which play a significant role in other studies (Lehner et al., 2020; Zhang and Chen, 2021), contribute minimally to scaling rates uncertainty. This may be because the changing rates of extreme precipitation do not depend heavily on the forcing scenarios, as extreme precipitation is primarily driven by the amount of moisture in the atmosphere which is related to total warming of climate models rather than the specific greenhouse gases or other forcing components (e.g., Li et al., 2021; Pendergrass et al., 2015; Senaviratne et al., 2016). On the other hand, scaling methods also play a substantial role in some regions, sometimes surpassing GCM contributions, highlighting their importance in scaling rate estimations, consistent with the findings of Ali et al. (2022) and Fowler et al. (2021). Moreover, this study indicates that an insufficient number of GCMs may pose challenges in achieving robust uncertainty decomposition. The analysis on quantifying the number of GCMs needed in the uncertainty decomposition framework suggests a recommendation that is only one GCM lower than that of Wang et al. (2020), who recommended using 10 GCMs for hydrological impact studies. Despite differences in frameworks and variables of interest, their results align closely with ours, reinforcing our recommendation. Although we suggest 9 GCMs as the optimal number for achieving robust results across the majority of regions and global averages for each simulation period, we recognize that certain regions exhibit notable variations. Specifically, ALA and WSA require 14 GCMs, NAS needs 13 GCMs, and SAF requires 10 GCMs.

In addition to our primary findings with CMIP6, we compare these results to those of CMIP5 at grid, regional, and temporal scales. In line with previous studies (Wu et al., 2024; Zhang and Chen, 2021), the grid-based analysis shows that CMIP5 and CMIP6 exhibit similar spatial patterns, with GCMs being the largest contributors to the uncertainty. However, regional differences in GCM contributions between CMIP5 and CMIP6 vary, with discrepancies exceeding 20 % in some regions. Notably, the average differences on a grid-based indicate that GCMs in CMIP5 contribute more than those in CMIP6, as well as in 15 out of 26 regions, suggesting that GCMs in CMIP6 have narrower spread compared to CMIP5. However, it should be noted that in regions where CMIP6 GCMs contribute more, the difference is smaller compared to regions where CMIP5 GCMs contribute more, leading to a negative average value, as seen in Fig. S13. This is a positive sign of improvement of the generation of CMIP, as a lower spread suggests lower uncertainty in the projected climate variables. Several studies have also demonstrated the lower spread of CMIP6 GCMs across various climate variables (Chen et al., 2021; Martel et al., 2022; Li et al., 2020). For regions and grids where GCMs in CMIP6 contribute more than those in CMIP5, this is likely due to the inclusion of more complex physical parameterizations in CMIP6 (Eyring et al., 2016), which may increase the model disagreement. Interestingly, the global average reveals little change in GCM contributions, but CMIP6 shows lower contributions from future emission scenarios in the far future, though the difference is negligible (about 1–2 %). This aligns with (Miao et al., 2023), who observed that by the end of the century, future emission scenarios in CMIP5 contributed more to runoff uncertainty than those in CMIP6.

5. Conclusion

This study aimed to understand the uncertainty in estimated scaling rates arising from three main sources: GCMs, future emission scenarios, and scaling methods, as well as their interactions within each source. The analysis began by estimating scaling rates for all 31 simulation periods from each GCM under all future emission scenarios and scaling methods for grids across the global land area. These grids were then aggregated to determine regional scaling for 26 regions. Using data

projected from 2040 to 2090 across 17 GCMs, three future emission scenarios, and three scaling methods, we analyzed 153 ensemble members for each grid and region. The uncertainty in the ensembles was decomposed into contributions from the three main sources and their interactions. Furthermore, the study evaluated the optimal number of GCMs needed for robust uncertainty decomposition by analyzing all possible GCM combinations. A comparison with CMIP5 was also conducted to better understand the differences between the two CMIP generations.

The findings of this study can be summarized as follows. First, the projected global scaling rates show a median with a slight decreasing trend over time, while regional scaling rates vary widely, encompassing both positive and negative values. Second, the uncertainty decomposition of scaling rates indicated that GCMs were the primary contributors to uncertainty across most regions, both at the grid and regional levels. While scaling methods and their interactions with GCMs also had a significant impact, future emission scenarios contributed minimally. Third, incorporating a large number of GCMs in the analysis can enhance its robustness, but it may also add to the computational load. Conversely, using too few GCMs can compromise the robustness of the results. The study systematically showed that incorporating fewer GCMs in the uncertainty decomposition framework led to an underestimation of GCM contributions and an overestimation of the effects of scaling methods and future emission scenarios. To ensure robust analysis, the study recommends including at least nine GCMs in future scaling projections. Lastly, comparisons between CMIP5 and CMIP6 revealed slight differences in uncertainty contributions from each source. For grid scaling, CMIP5 exhibited higher uncertainty contributions from main sources compared to CMIP6, which had more significant interaction effects. In regional scaling, while differences varied by region, no substantial global differences were observed.

While our study provides valuable insights into the sources of uncertainty in scaling rates, several limitations should be considered, as they may influence the interpretation of our findings. First and foremost, our study focuses exclusively on the changing rates of extreme precipitation in relation to dew point temperature, which is just one of several thermodynamic factors; others include pressure and the moist-adiabatic lapse rate of the air parcel (Gu et al., 2023). Although dew point temperature has proven effective in explaining these changing rates (Ali et al., 2018; Fowler et al., 2021), it is important to recognize that dynamic factors, such as vertical velocity, also play a significant role in influencing scaling rates (Gu et al., 2023; Pfahl et al., 2017; Ritzhaupt and Maraun, 2024; Ngai et al., 2024). Additionally, for future climate projections, uncertainty in scaling rates may also arise from the internal variability of each GCM (John et al., 2022), suggesting that differences in the initial states of each GCM could introduce additional variability into the modeling process. Therefore, future studies should consider incorporating internal variability into impact modeling to achieve a more comprehensive understanding of uncertainties. Moreover, when expanding the study to more regions or incorporating additional thermodynamic factors, it is recommended to assess their effect on uncertainty decomposition and use at least nine GCMs to maintain robustness. Despite these limitations, we believe this paper takes meaningful steps toward quantifying the influence of scaling rate projections, ultimately aiding policymakers and stakeholders in planning future water policies.

CRediT authorship contribution statement

Min Sothearith: Writing – original draft, Methodology, Investigation, Formal analysis, Data curation. **Kuk-Hyun Ahn:** Writing – review & editing, Visualization, Validation, Supervision, Resources, Project administration, Methodology.

Declaration of competing interest

The authors declare the following financial interests/personal

relationships which may be considered as potential competing interests: Kuk-Hyun Ahn reports financial support was provided by National Research Foundation of Korea. If there are other authors, they declare that they have no known competing financial interests or personal relationships that could have appeared to influence the work reported in this paper.

Acknowledgment

This work was supported by the National Research Foundation of Korea (NRF) grant funded by the Korea government (MSIT) (No. RS-2023-00208210).

Appendix A. Supplementary data

Supplementary data to this article can be found online at <https://doi.org/10.1016/j.jhydrol.2025.133260>.

Data availability

Data will be made available on request.

References

- Alduchov, O.A., Eskridge, R.E., 1996. Improved Magnus Form Approximation of Saturation Vapor Pressure. *J. Appl. Meteor.* 35, 601–609. [https://doi.org/10.1175/1520-0450\(1996\)035<0601:IMFAOS>2.0.CO;2](https://doi.org/10.1175/1520-0450(1996)035<0601:IMFAOS>2.0.CO;2).
- Ali, H., Fowler, H.J., Mishra, V., 2018. Global Observational Evidence of Strong Linkage Between Dew Point Temperature and Precipitation Extremes. *Geophys. Res. Lett.* 45, 12320–12330. <https://doi.org/10.1029/2018GL080557>.
- Ali, H., Fowler, H.J., Pritchard, D., Lenderink, G., Blenkinsop, S., Lewis, E., 2022. Towards Quantifying the Uncertainty in Estimating Observed Scaling Rates. *Geophys. Res. Lett.* 49, e2022GL099138. <https://doi.org/10.1029/2022GL099138>.
- Ali, H., Mishra, V., 2017. Contrasting response of rainfall extremes to increase in surface air and dewpoint temperatures at urban locations in India. *Sci Rep* 7, 1228. <https://doi.org/10.1038/s41598-017-01306-1>.
- Allan, R.P., Soden, B.J., 2008. Atmospheric Warming and the Amplification of Precipitation Extremes. *Science* 321, 1481–1484. <https://doi.org/10.1126/science.1160787>.
- Archer, G.E.B., Saltelli, A., Sobol, I.M., 1997. Sensitivity measures,anova-like Techniques and the use of bootstrap. *J. Stat. Comput. Simul.* 58, 99–120. <https://doi.org/10.1080/00949659708811825>.
- Barbero, R., Westra, S., Lenderink, G., Fowler, H.J., 2018. Temperature-extreme precipitation scaling: a two-way causality? *Int. J. Climatol.* 38, e1274–e1279. <https://doi.org/10.1002/joc.5370>.
- Buathongkhue, C., Sureeya, K., Kaewthong, N., 2024. Analysis and Prediction of Rainfall with Oceanic Niño Index and Climate Variables Using Correlation Coefficient and Deep Learning. *Civil Engineering Journal* 10, 1354–1369. <https://doi.org/10.28991/CEJ-2024-010-05-01>.
- Chen, C.-A., Hsu, H.-H., Liang, H.-C., 2021. Evaluation and comparison of CMIP6 and CMIP5 model performance in simulating the seasonal extreme precipitation in the Western North Pacific and East Asia. *Weather Clim. Extremes* 31, 100303. <https://doi.org/10.1016/j.wace.2021.100303>.
- Clapeyron, E., 1834. Mémoire sur la puissance motrice de la chaleur. de l' Ecole Polytechnique XIV, 153–191.
- Clausius, R., 1850. Ueber die bewegende Kraft der Wärme und die Gesetze, welche sich daraus für die Wärmelehre selbst ableiten lassen. *Ann. Phys.* 155, 368–397. <https://doi.org/10.1002/andp.18501550306>.
- Cleveland, W.S., 1979. Robust Locally Weighted Regression and Smoothing Scatterplots. *J. Am. Stat. Assoc.* 74, 829–836. <https://doi.org/10.1080/01621459.1979.10481038>.
- Deng, A.A.N., Nursetiawan, I.J., Riyadi, S., Zaki, A., 2024. Intelligent Forecasting of Flooding Intensity Using Machine Learning. *Civil Eng. J.* 10, 3269–3291. <https://doi.org/10.28991/CEJ-2024-010-010-010>.
- Eyring, V., Bony, S., Meehl, G.A., Senior, C.A., Stevens, B., Stouffer, R.J., Taylor, K.E., 2016. Overview of the Coupled Model Intercomparison Project Phase 6 (CMIP6) experimental design and organization. *Geosci. Model Dev.* 9, 1937–1958. <https://doi.org/10.5194/gmd-9-1937-2016>.
- Fischer, E.M., Knutti, R., 2016. Observed heavy precipitation increase confirms theory and early models. *Nature Clim Change* 6, 986–991. <https://doi.org/10.1038/nclimate3110>.
- Fowler, H.J., Lenderink, G., Prein, A.F., Westra, S., Allan, R.P., Ban, N., Barbero, R., Berg, P., Blenkinsop, S., Do, H.X., Guerreiro, S., Haerter, J.O., Kendon, E.J., Lewis, E., Schaer, C., Sharma, A., Villarini, G., Wasko, C., Zhang, X., 2021. Anthropogenic intensification of short-duration rainfall extremes. *Nat Rev Earth Environ* 2, 107–122. <https://doi.org/10.1038/s43017-020-00128-6>.
- Gu, L., Yin, J., Gentine, P., Wang, H.-M., Slater, L.J., Sullivan, S.C., Chen, J., Zschieschler, J., Guo, S., 2023. Large anomalies in future extreme precipitation sensitivity driven by atmospheric dynamics. *Nat Commun* 14, 3197. <https://doi.org/10.1038/s41467-023-39039-7>.
- Hardwick Jones, R., Westra, S., Sharma, A., 2010. Observed relationships between extreme sub-daily precipitation, surface temperature, and relative humidity. *Geophys. Res. Lett.* 37. <https://doi.org/10.1029/2010GL045081>.
- Hawkins, E., Sutton, R., 2009. The Potential to Narrow Uncertainty in Regional Climate Predictions. *Bull. Am. Meteorol. Soc.* 90, 1095–1108. <https://doi.org/10.1175/2009BAMS2607.1>.
- IPCC, 2021. Climate Change 2021: The Physical Science Basis. Contribution of Working Group I to the Sixth Assessment Report of the Intergovernmental Panel on Climate Change, 1st ed. Cambridge University Press. Doi: 10.1017/9781009157896.
- Ji, Y., Fu, J., Liu, B., Huang, Z., Tan, X., 2024. Uncertainty separation of drought projection in the 21st century using SMILEs and CMIP6. *J. Hydrol.* 628, 130497. <https://doi.org/10.1016/j.jhydrol.2023.130497>.
- John, A., Douville, H., Ribes, A., Yiou, P., 2022. Quantifying CMIP6 model uncertainties in extreme precipitation projections. *Weather Clim. Extremes* 36, 100435. <https://doi.org/10.1016/j.wace.2022.100435>.
- Kharin, V.V., Zwiers, F.W., Zhang, X., Hegerl, G.C., 2007. Changes in Temperature and Precipitation Extremes in the IPCC Ensemble of Global Coupled Model Simulations. *J. Clim.* 20, 1419–1444. <https://doi.org/10.1175/JCLI4066.1>.
- Kharin, V.V., Zwiers, F.W., Zhang, X., Wehner, M., 2013. Changes in temperature and precipitation extremes in the CMIP5 ensemble. *Clim. Change* 119, 345–357. <https://doi.org/10.1007/s10584-013-0705-8>.
- Knutti, R., Baumberger, C., Hirsch Hadorn, G., 2019. Uncertainty Quantification Using Multiple Models—Prospects and Challenges. In: Beisbart, C., Saam, N.J. (Eds.), *Computer Simulation Validation: Fundamental Concepts, Methodological Frameworks, and Philosophical Perspectives*. Springer International Publishing, Cham, pp. 835–855. https://doi.org/10.1007/978-3-319-70766-2_34.
- Kuma, P., Bender, F.-A.-M., Jónsson, A.R., 2023. Climate Model Code Genealogy and Its Relation to Climate Feedbacks and Sensitivity. *J. Adv. Model. Earth Syst.* 15, e2022MS003588. <https://doi.org/10.1029/2022MS003588>.
- Lehner, F., Deser, C., Maher, N., Marotzke, J., Fischer, E.M., Brunner, L., Knutti, R., Hawkins, E., 2020. Partitioning climate projection uncertainty with multiple large ensembles and CMIP5/6. *Earth Syst. Dyn.* 11, 491–508. <https://doi.org/10.5194/esd-11-491-2020>.
- Lenderink, G., Attema, J., 2015. A simple scaling approach to produce climate scenarios of local precipitation extremes for the Netherlands. *Environ. Res. Lett.* 10, 085001. <https://doi.org/10.1088/1748-9326/10/8/085001>.
- Lenderink, G., Mok, H.Y., Lee, T.C., van Oldenborgh, G.J., 2011. Scaling and trends of hourly precipitation extremes in two different climate zones – Hong Kong and the Netherlands. *Hydroclim. Earth Syst. Sci.* 15, 3033–3041. <https://doi.org/10.5194/hess-15-3033-2011>.
- Lenderink, G., van Meijgaard, E., 2008. Increase in hourly precipitation extremes beyond expectations from temperature changes. *Nature Geosci* 1, 511–514. <https://doi.org/10.1038/ngeo262>.
- Li, S.-Y., Miao, L.-J., Jiang, Z.-H., Wang, G.-J., Gnyawali, K.R., Zhang, J., Zhang, H., Fang, K., He, Y., Li, C., 2020. Projected Drought Conditions in Northwest China with CMIP6 Models under Combined SSPs and RCPs for 2015–2099. Advances in Climate Change Research, including Special Topic on East Asian Climate Response to 1.5°C Global Warming 11, 210–217. <https://doi.org/10.1016/j.accre.2020.09.003>.
- Li, C., Zwiers, F., Zhang, X., Li, G., Sun, Y., Wehner, M., 2021. Changes in Annual Extremes of Daily Temperature and Precipitation in CMIP6 Models. *J. Clim.* 34, 3441–3460. <https://doi.org/10.1175/JCLI-D-19-1013.1>.
- Liang-Liang, L., Jian, L., Ru-Cong, Y., 2022. Evaluation of CMIP6 HighResMIP models in simulating precipitation over Central Asia. *Adv. Clim. Chang. Res.* 13, 1–13. <https://doi.org/10.1016/j.accre.2021.09.009>.
- Martel, J.-L., Brissette, F., Troin, M., Arsenault, R., Chen, J., Su, T., Lucas-Picher, P., 2022. CMIP5 and CMIP6 Model Projection Comparison for Hydrological Impacts Over North America. *Geophys. Res. Lett.* 49, e2022GL098364. <https://doi.org/10.1029/2022GL098364>.
- Martinkova, M., Kysely, J., 2020. Overview of Observed Clausius-Clapeyron Scaling of Extreme Precipitation in Midlatitudes. *Atmos.* 11, 786. <https://doi.org/10.3390/atmos11080786>.
- Miao, C., Wu, Y., Fan, X., Su, J., 2023. Projections of Global Land Runoff Changes and Their Uncertainty Characteristics During the 21st Century. *Earth's Future* 11, e2022EF003286. <https://doi.org/10.1029/2022EF003286>.
- Mishra, V., Wallace, J.M., Lettenmaier, D.P., 2012. Relationship between hourly extreme precipitation and local air temperature in the United States. *Geophys. Res. Lett.* 39, https://doi.org/10.1029/2012GL052790.
- Molnar, P., Fatici, S., Gaál, L., Szolgay, J., Burlando, P., 2015. Storm type effects on super Clausius-Clapeyron scaling of intense rainstorm properties with air temperature. *Hydroclim. Earth Syst. Sci.* 19, 1753–1766. <https://doi.org/10.5194/hess-19-1753-2015>.
- Ngai, S.T., Raghavan, V.S., Chung, J.X., Ona, B.J., Kimbrell, L.T., Nguyen, N.S., Nguyen, T.-H., Liu, S., 2024. Relative contribution of dynamic and thermodynamic components on Southeast Asia future precipitation changes from different multi-GCM ensemble members. *Adv. Clim. Chang. Res.* <https://doi.org/10.1016/j.accre.2024.08.007>.
- O’Gorman, P.A., 2015. Precipitation Extremes Under Climate Change. *Curr. Clim. Change Rep.* 1, 49–59. <https://doi.org/10.1007/s40641-015-0009-3>.
- O’Gorman, P.A., Schneider, T., 2009. Scaling of Precipitation Extremes over a Wide Range of Climates Simulated with an Idealized GCM. *J. Clim.* 22, 5676–5685. <https://doi.org/10.1175/2009JCLI2701.1>.
- O’Neill, B.C., Tebaldi, C., van Vuuren, D.P., Eyring, V., Friedlingstein, P., Hurtt, G., Knutti, R., Kriegler, E., Lamarque, J.-F., Lowe, J., Meehl, G.A., Moss, R., Riahi, K., Sanderson, B.M., 2016. The Scenario Model Intercomparison Project (ScenarioMIP)

- for CMIP6. *Geosci. Model Dev.* 9, 3461–3482. <https://doi.org/10.5194/gmd-9-3461-2016>.
- Park, I.-H., Min, S.-K., 2017. Role of Convective Precipitation in the Relationship between Subdaily Extreme Precipitation and Temperature. *J. Clim.* 30, 9527–9537. <https://doi.org/10.1175/JCLI-D-17-0075.1>.
- Pathak, R., Dasari, H.P., Ashok, K., Hoteit, I., 2023. Effects of multi-observations uncertainty and models similarity on climate change projections. *Npj Clim Atmos Sci* 6, 1–12. <https://doi.org/10.1038/s41612-023-00473-5>.
- Pendergrass, A.G., Lehner, F., Sanderson, B.M., Xu, Y., 2015. Does extreme precipitation intensity depend on the emissions scenario? *Geophys. Res. Lett.* 42, 8767–8774. <https://doi.org/10.1002/2015GL065854>.
- Pfahl, S., O'Gorman, P.A., Fischer, E.M., 2017. Understanding the regional pattern of projected future changes in extreme precipitation. *Nature Clim Change* 7, 423–427. <https://doi.org/10.1038/nclimate3287>.
- Pumo, D., Carlini, G., Blenkinsop, S., Arnone, E., Fowler, H., Noto, L.V., 2019. Sensitivity of extreme rainfall to temperature in semi-arid Mediterranean regions. *Atmos. Res.* 225, 30–44. <https://doi.org/10.1016/j.atmosres.2019.03.036>.
- Riahi, K., van Vuuren, D.P., Kriegler, E., Edmonds, J., O'Neill, B.C., Fujimori, S., Bauer, N., Calvin, K., Dellink, R., Fricko, O., Lutz, W., Popp, A., Cuartero, J.C., Kc, S., Leimbach, M., Jiang, L., Kram, T., Rao, S., Emmerling, J., Ebi, K., Hasegawa, T., Havlik, P., Humpenöder, F., Da Silva, L.A., Smith, S., Stehfest, E., Bosetti, V., Eom, J., Gernaat, D., Masui, T., Rogelj, J., Strefler, J., Drouet, L., Krey, V., Luderer, G., Harmsen, M., Takahashi, K., Baumstark, L., Doelman, J.C., Kainuma, M., Klimont, Z., Marangoni, G., Lotze-Campen, H., Obersteiner, M., Tabeau, A., Tavoni, M., 2017. The Shared Socioeconomic Pathways and their energy, land use, and greenhouse gas emissions implications: An overview. *Glob. Environ. Chang.* 42, 153–168. <https://doi.org/10.1016/j.gloenvcha.2016.05.009>.
- Ritzhaupt, N., Maraun, D., 2024. State-of-the-art climate models reduce dominant dynamical uncertainty in projections of extreme precipitation. *Environ. Res.: Climate* 3, 021001. <https://doi.org/10.1088/2752-5295/ad2eb2>.
- Saltelli, A., Annoni, P., Azzini, I., Campolongo, F., Ratto, M., Tarantola, S., 2010. Variance based sensitivity analysis of model output. Design and estimator for the total sensitivity index. *Comput. Phys. Commun.* 181, 259–270. <https://doi.org/10.1016/j.cpc.2009.09.018>.
- Sansom, P.G., Stephenson, D.B., Ferro, C.A.T., Zappa, G., Shaffrey, L., 2013. Simple Uncertainty Frameworks for Selecting Weighting Schemes and Interpreting Multimodel Ensemble Climate Change Experiments. <https://doi.org/10.1175/JCLI-D-12-00462.1>.
- Schroere, K., Kirchengast, G., 2018. Sensitivity of extreme precipitation to temperature: the variability of scaling factors from a regional to local perspective. *Clim Dyn* 50, 3981–3994. <https://doi.org/10.1007/s00382-017-3857-9>.
- Seneviratne, S.I., Donat, M.G., Pitman, A.J., Knutti, R., Wilby, R.L., 2016. Allowable CO₂ emissions based on regional and impact-related climate targets. *Nature* 529, 477–483. <https://doi.org/10.1038/nature16542>.
- Seneviratne, S.I., Nicholls, N., Easterling, D., Goodess, C.M., Kanae, S., Kossin, J., Luo, Y., Marengo, J., McInnes, K., Rahimi, M., Reichstein, M., Sorteberg, A., Vera, C., Zhang, X., Rusticucci, M., Semenov, V., Alexander, L.V., Allen, S., Benito, G., Cavazos, T., Clague, J., Conway, D., Della-Marta, P.M., Gerber, M., Gong, S., Goswami, B.N., Hemer, M., Huggel, C., Van Den Hurk, B., Kharin, V.V., Kitoh, A., Tank, A.M.G.K., Li, G., Mason, S., McGuire, W., Van Oldenborgh, G.J., Orlowsky, B., Smith, S., Thiaw, W., Velegrakis, A., Yiou, P., Zhang, T., Zhou, T., Zwiers, F.W., 2012. Changes in Climate Extremes and their Impacts on the Natural Physical Environment, in: Field, C.B., Barros, V., Stocker, T.F., Dahe, Q. (Eds.), *Managing the Risks of Extreme Events and Disasters to Advance Climate Change Adaptation*. Cambridge University Press, pp. 109–230. Doi: 10.1017/CBO9781139177245.006.
- Sobel, I.M., 1990. On sensitivity estimation for nonlinear mathematical models. *Matem. Mod.* 2, 112–118.
- Trenberth, K.E., 2011. Changes in precipitation with climate change. *Climate Res.* 47, 123–138. <https://doi.org/10.3354/cr00953>.
- Trenberth, K.E., Dai, A., Rasmusson, R.M., Parsons, D.B., 2003. The Changing Character of Precipitation. *Bull. Am. Meteorol. Soc.* 84, 1205–1218. <https://doi.org/10.1175/BAMS-84-9-1205>.
- Utsumi, N., Seto, S., Kanae, S., Maeda, E.E., Oki, T., 2011. Does higher surface temperature intensify extreme precipitation? *Geophys. Res. Lett.* 38. <https://doi.org/10.1029/2011GL048426>.
- Van de Vyver, H., Van Schaeybroeck, B., De Troch, R., Hamdi, R., Termonia, P., 2019. Modeling the Scaling of Short-Duration Precipitation Extremes With Temperature. *Earth Space Sci.* 6, 2031–2041. <https://doi.org/10.1029/2019EA000665>.
- Wang, H.-M., Chen, J., Xu, C.-Y., Zhang, J., Chen, H., 2020. A Framework to Quantify the Uncertainty Contribution of GCMs Over Multiple Sources in Hydrological Impacts of Climate Change. *Earth's Future* 8, e2020EF001602. <https://doi.org/10.1029/2020EF001602>.
- Wang, G., Sun, X., 2022. Monotonic Increase of Extreme Precipitation Intensity With Temperature When Controlled for Saturation Deficit. *Geophys. Res. Lett.* 49, e2022GL097881. <https://doi.org/10.1029/2022GL097881>.
- Wasko, C., Sharma, A., 2014. Quantile regression for investigating scaling of extreme precipitation with temperature. *Water Resour. Res.* 50, 3608–3614. <https://doi.org/10.1002/2013WR015194>.
- Wasko, C., Lu, W.T., Mehrotra, R., 2018. Relationship of extreme precipitation, dry-bulb temperature, and dew point temperature across Australia. *Environ. Res. Lett.* 13, 074031. <https://doi.org/10.1088/1748-9326/aad135>.
- Westra, S., Fowler, H.J., Evans, J.P., Alexander, L.V., Berg, P., Johnson, F., Kendon, E.J., Lenderink, G., Roberts, N.M., 2014. Future changes to the intensity and frequency of short-duration extreme rainfall. *Rev. Geophys.* 52, 522–555. <https://doi.org/10.1002/2014RG000464>.
- Wu, Y., Miao, C., Slater, L., Fan, X., Chai, Y., Sorooshian, S., 2024. Hydrological Projections under CMIP5 and CMIP6: Sources and Magnitudes of Uncertainty. *Bull. Am. Meteorol. Soc.* 105, E59–E74. <https://doi.org/10.1175/BAMS-D-23-0104.1>.
- Yanfatianni, E., Marzuki, M., Vonnisa, M., Razli, P., Hapsoro, C.A., Ramadhan, R., Yusnaini, H., 2024. Extreme Rainfall Trends and Hydrometeorological Disasters in Tropical Regions: Implications for Climate Resilience. *Emerg. Sci. J.* 8, 1860–1874. <https://doi.org/10.28991/ESJ-2024-08-05-012>.
- Yip, S., Ferro, C.A.T., Stephenson, D.B., Hawkins, E., 2011. A Simple, Coherent Framework for Partitioning Uncertainty in Climate Predictions. *J. Climate* 24, 4634–4643. <https://doi.org/10.1175/2011JCLI4085.1>.
- Yoo, S., Ahn, K.-H., 2023. Understanding extreme precipitation scaling with temperature: insights from multi-spatiotemporal analysis in South Korea. *Environ. Res. Lett.* 18, 124032. <https://doi.org/10.1088/1748-9326/ad0afa>.
- Zhang, S., Chen, J., 2021. Uncertainty in Projection of Climate Extremes: A Comparison of CMIP5 and CMIP6. *J. Meteorol. Res.* 35, 646–662. <https://doi.org/10.1007/s13351-021-1012-3>.
- Zhang, W., Villarini, G., Wehner, M., 2019. Contrasting the responses of extreme precipitation to changes in surface air and dew point temperatures. *Clim. Change* 154, 257–271. <https://doi.org/10.1007/s10584-019-02415-8>.
- Zhang, S., Zhou, Z., Peng, P., Xu, C., 2023. A New Framework for Estimating and Decomposing the Uncertainty of Climate Projections. *J. Clim.* 37, 365–384. <https://doi.org/10.1175/JCLI-D-23-0064.1>.
- Zhang, X., Zwiers, F.W., Li, G., Wan, H., Cannon, A.J., 2017. Complexity in estimating past and future extreme short-duration rainfall. *Nature Geosci.* 10, 255–259. <https://doi.org/10.1038/geo2911>.